JOURNAL OF GEOPHYSICAL RESEARCH, VOL. 107, NO. D10, 10.1029/2001JD001048, 2002

# Distribution and influence of convection in the tropical tropopause region

A. Gettelman
National Center for Atmospheric Research, Boulder, Colorado, USA

M. L. Salby
Program in Atmospheric and Oceanic Sciences, University of Colorado, Boulder, Colorado, USA

F. Sassi
National Center for Atmospheric Research, Boulder, Colorado, USA

Received 25 June 2001; revised 26 September 2001; accepted 28 September 2001; published 21 May 2002.

[1] A global analysis of convective cloud in the tropical tropopause region (12–17 km) is presented. The analysis is based on high-resolution global imagery of cloud brightness temperatures from satellites and from contemporaneous reanalysis temperatures. The coverage by deep convection decreases nearly exponentially with increasing altitude in the tropopause region. Convection is found at temperatures colder than the tropical cold point tropopause over ~0.5% (±0.25%) of the tropics. Convection rarely penetrates more than 1.5 km above the tropopause. Large-scale relationships between cold tropopause temperatures and deep convection indicate that where the tropopause is coldest convection penetrates most frequently. Small-scale relationships show that the coldest diurnal tropopause temperatures occur after the diurnal peak in deep convection at tropopause levels over land. The coverage by deep convection is used to estimate the mass exchange or turnover time due to convection in the tropopause region. This turnover time is of the order of weeks at 12 km but increases to longer than a year at 18 km, with significant uncertainties in the tropopause region. *INDEX TERMS:* 3314 Meteorology and Atmospheric Dynamics: Convective processes; 3362 Meteorology and Atmospheric Dynamics: Stratosphere/troposphere interactions; 0341 Atmospheric Composition and Structure: Middle atmosphere-constituent transport and chemistry (3334); *KEYWORDS:* tropical convection, stratosphere-troposphere exchange

## 1. Introduction and Motivation

[2] *Brewer* [1949] and *Dobson et al.* [1946] hypothesized that air enters the stratosphere through the tropical tropopause. This air populates the stratosphere and regulates the radiative and chemical balance of the stratosphere by carrying trace species with it. The role of tropical deep convection in this process remains an important uncertainty [*Holton et al.*, 1995]. Understanding the influence of convection on the exchange of air between the stratosphere and the troposphere is thus critical for understanding the chemical composition of the stratosphere. The processing of air by convection may strongly affect the water vapor distribution of the tropopause region [*Danielsen*, 1982; *Holton et al.*, 1995; *Sherwood and Dessler*, 2001]. It certainly affects trace species produced at the surface that may be rapidly lofted into the stratosphere. As evidence, *Kritz et al.* [1993] observed radon ($^{222}$Rn), a gas with a surface source and a lifetime of 4 days, in the tropical stratosphere near active regions of deep convection.

[3] The tropical tropopause region is defined as the region between the main convective outflow (~12 km or 200 hPa) and the cold point of the temperature profile, (~17 km). As discussed by *Atticks and Robinson* [1983] and more recently by *Highwood and Hoskins* [1998], the tropopause in the tropics is not a material surface but a transition zone between the troposphere and the stratosphere. Convection represents a potentially dominant source of lower tropospheric air in the tropopause region.


0148-0227/02/2001JD001048$09.00

[4] Previous studies have observed convection near or above the tropical tropopause. *Zhang* [1993] analyzed the seasonal cycle of cloud brightness temperature data using satellites in several longitude sectors in the tropics. *Soden* [2000] looked at deep convection above the tropopause and its relationship to the diurnal cycle, based on the method of *Schmetz et al.* [1997], for 3 months over South and Central America. *Roca and Ramanathan* [2000] examined the organization of convection in the Indian Ocean.

[5] In this work we seek to better understand the role of tropical deep convection that penetrates into the tropopause region. Observations of cloud from satellite brightness temperature, along with analyses of atmospheric temperature, are used to locate cloud tops in the tropical upper troposphere and lower stratosphere. In section 2.1 the methodology and data sets are described. Section 2.2 details and quantifies some of the key uncertainties. Section 3 describes the distribution of convective events in the tropopause region and in particular those events that are colder than the analyzed cold point tropopause. The small-scale relationship between the cold point tropopause and convection is examined in section 4. In section 5 a method is developed for estimating the time for convection to replace the mass in the tropopause region. Conclusions are presented in section 6.

## 2. Data and Methodology

### 2.1. Cloud and Tropopause

[6] To determine the position of deep convection in the tropopause region, cloud brightness temperatures observed from satellites are compared with analyzed tropopause temperatures. Satellite

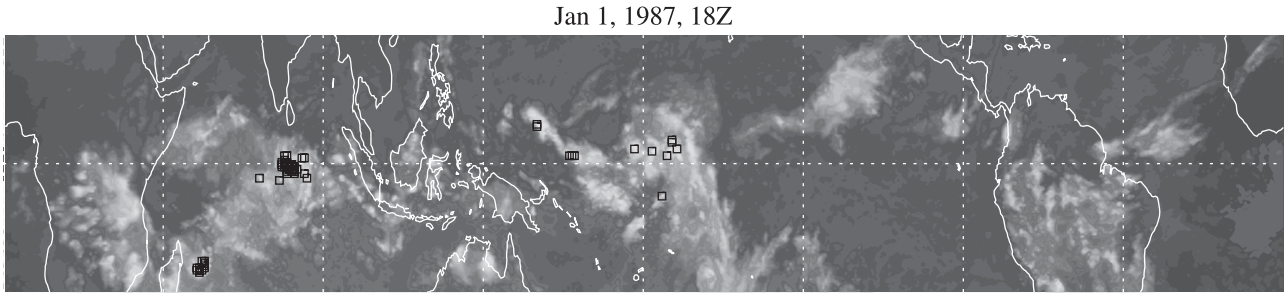


**Figure 1.** Brightness temperatures for the region of the tropics between 20°S and 20°N for 1 January 1987 at 1800 UT (UTC). Small squares indicate the locations of those temperatures colder than the local cold point tropopause. Grayscale range is from 340°K (black) to 175°K (white).

brightness temperature is represented at high space-time resolution in global cloud imagery (GCI), described by *Salby et al.* [1991]. This data set has a resolution of ~0.5° latitude, ~0.5° longitude, and 3 hours in time with complete coverage of the Earth. As described by *Salby et al.* [1991], the GCI images are derived from 11-μm satellite infrared radiance measurements with a footprint of 8 km. The data have continuous, synoptic coverage. Construction of the GCI and their validation are discussed by *Tanaka et al.* [1991]. Data are investigated here over 3.5 years: from October 1986 to February 1989 and October 1991 to September 1992. These data have also been used by *Bergman and Salby* [1994] to study equatorial waves, *Liebmann et al.* [1994] to study the organization of tropical convection, and *Sassi et al.* [2001] to study the relationship between deep convection and upper tropospheric humidity.

[7] To determine where clouds lie in relation to the tropopause, atmospheric thermal structure is diagnosed from the reanalyses developed by the National Centers for Environmental Prediction (NCEP) and the National Center for Atmospheric Research (NCAR), which are described by *Kalnay et al.* [1996]. We define the tropical tropopause as the cold point of a vertical profile, the cold point tropopause (CPT). This criterion is only one of several possible definitions of the tropical tropopause [*Newell and Gould-Stewart*, 1981; *Holton et al.*, 1995; *Selkirk*, 1993; *Zhou et al.*, 2001]. The cold point is well suited for the analysis because it is easily identifiable. The CPT is also important for limiting the transport of water vapor into the stratosphere.

[8] To calculate the CPT, we adopt the method used by *Hoinka* [1998] and *Kochanski* [1955] to extrapolate tropopause temperature from standard pressure level data. The lapse rate immediately above and below the general location of the tropical tropopause is extrapolated linearly, the analyzed CPT temperature being found at the intersection of these lines. The absolute value and spatial and seasonal variation of the NCEP CPT temperature are similar to the CPT observed with radiosondes [*Seidel et al.*, 2001]. Therefore analyzed CPT temperatures do not suffer from the warm bias of the analyzed thermal tropopause noted by *Randel et al.* [2000]. Calculated on a 2° latitude × 2.5° longitude grid every 6 hours, the CPT is interpolated to the higher resolution of the GCI in both time (3 hours) and space (0.5°). The analyzed tropopause in the tropics varies slowly in time and space on this scale, so the interpolation does not introduce aliasing.

[9] A sample of brightness temperatures below the tropopause is illustrated in Figure 1 for an individual cloud image. Brightness temperature for the region of the tropics between 20°S and 20°N is shaded, with squares indicating where temperatures are colder than the analyzed CPT. There are clusters of points over the Indian Ocean and the central Pacific. The fractional coverage of clouds colder than the tropopause in this image (56 points) is ~0.1%. This analysis differs from the dual-channel brightness temperature approach of *Schmetz et al.* [1997] because it also provides cloud height relative to the tropopause as a temperature difference.

### 2.2. Uncertainties

[10] Convective events occur on time and space scales even smaller than resolved by the GCI. Updrafts and penetrating towers are typically at 1–10 km in diameter [*Fujita*, 1992]. The timescale of convective penetration events may be as short as 10 min [*Fujita*, 1992]. GCI temperatures reflect an average of 8-km observations within ±90 min. Differences in scale introduce uncertainties into the estimation of cloud fraction. Four uncertainties are considered: spatial averaging of the 8-km observations in the GCI data, temporal averaging of the 8-km observations in the GCI data, the position of cloud top relative to its brightness temperature, and the difference between the actual cloud temperature and its environment.

[11] First, we examine the effect of averaging 8-km data in the GCI. Individual pixels in GCI are 3-hour samples of 8-km observations. A histogram of GCI pixels is compared in Figure 2a against that of the raw 8-km pixels. A slight bias to the GCI averaging is evident in Figure 2a. The histogram of GCI brightness temperatures is higher in the middle of the distribution and lower at the tails than the histogram of the 8-km raw data. Figure 2b illustrates this bias in the ratio of GCI averaged data frequency to the actual 8-km frequency for temperature bins up to 240°K. At temperatures colder than 215°K, there is a fall off in the ratio. It decreases to under 0.5 at the coldest temperatures, where 50-km pixels of GCI are sparsely populated by 8-km cloud pixels. Figure 2c indicates that the fraction of clouds colder than a given temperature is less in the GCI than in the raw 8-km data for all temperatures colder than 240°K. This difference is of the order of 0.5% of the fractional coverage. It is insignificant at lower levels, but the difference becomes important at temperatures near the CPT, where the fractional coverage decreases below 1%.

[12] A stochastic model of cloud events has been constructed to quantify the sampling uncertainties (Appendix A). It samples a random brightness temperature field as the satellites do. Undersampling becomes significant near the CPT, when cloud fraction decreases to less than 1%. At tropopause levels, actual cloud fraction may be double what is represented in the GCI data. The temporal sampling introduces a further uncertainty of about ±30% in the estimation of cloud fractions at tropopause levels. Furthermore, cloud top temperatures are usually several degrees colder than brightness temperatures, because infrared (IR) emissions come from below cloud top. On the other hand, clouds overshooting their level of neutral buoyancy are colder than the environment. In a statistical analysis of many events (pixels) such as this work, these systematic biases in different directions partially cancel. They do not necessarily cancel in each case.

[13] We conclude from these analyses that the brightness temperature is a fairly good estimator of the cloud top when compared to analyzed temperatures, but with some range of

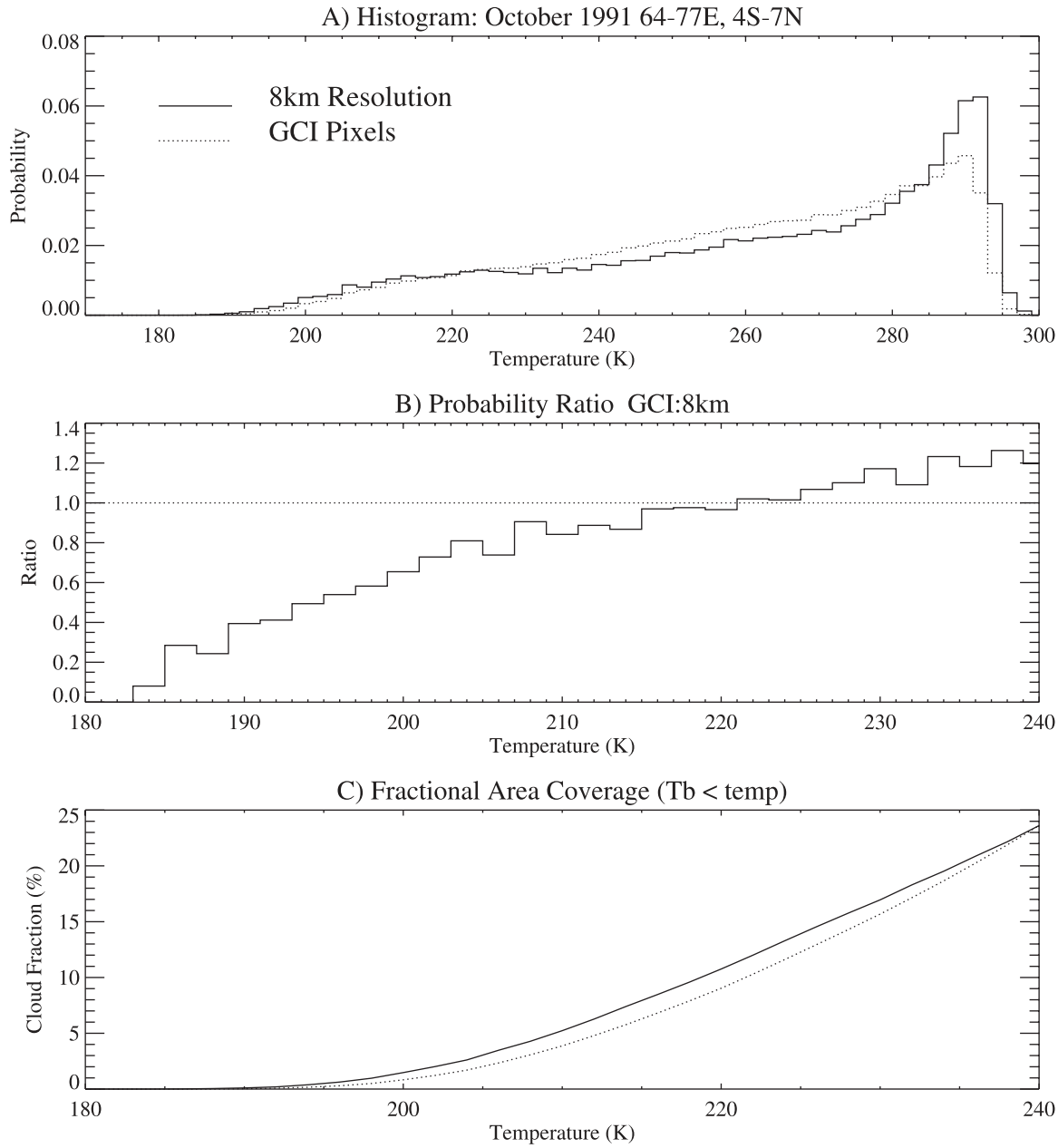


**Figure 2.** (a) Normalized histogram of brightness temperatures for October 1991 in the region from 64°–77°E and 4°S–7°N. (b) Ratio of GCI probability to 8-km probability in Figure 2a for the coldest temperatures (note different temperature scale from Figure 2a). Dotted line is 1:1 line. (c) Cumulative distribution of cloud fraction colder than a given temperature threshold for the same region as Figure 2a. In Figures 2a and 2c the solid line is from the 8-km data, and the dotted line is from the GCI pixels.

uncertainties, particularly near the CPT. A more detailed and quantitative discussion of uncertainties is given in the Appendix A.

## 3. Location of Deep Convection

[14] The GCI's high space and time resolution enables it to capture the dominant scales of organized convection. Our analysis focuses on clouds above 200 hPa, which is near 220°–215°K.

[15] The fractional area covered by cloud ($\eta$) with temperatures colder than 215°K ($\eta_{215}$) is illustrated in Figure 3. As discussed in section 2.2, the actual cloud fraction is probably 0.5% greater. Seasonally averaged $\eta_{215}$ has maxima over the continents and the Intertropical Convergence Zone (ITCZ) during local summer. In general, the summer hemisphere has far more convective activity reaching 215°K than the winter hemisphere, and the maxima in $\eta_{215}$ are typically centered off the equator. The greatest values of $\eta_{215}$ are associated with the South Asian Monsoon in July–September, with values nearly as great over Central America during these same months.

[16] The fraction of cold cloud has been calculated for various levels in the tropics ($\eta(t)$). Figure 4 displays zonal mean $\eta(t)$ for 2 months as a function of latitude and temperature. Zonal mean CPT temperature (dashed) is also plotted in Figure 4. Note that temperature serves as a pseudovertical coordinate, decreasing upward. During both months, $\overline{\eta}(t)$ is a maximum for all temperatures in the summer hemisphere at ~10° from the equator. The edge of winter storm activity in midlatitudes is visible at 25°–30° latitude in the winter hemisphere. The tropopause is colder during February

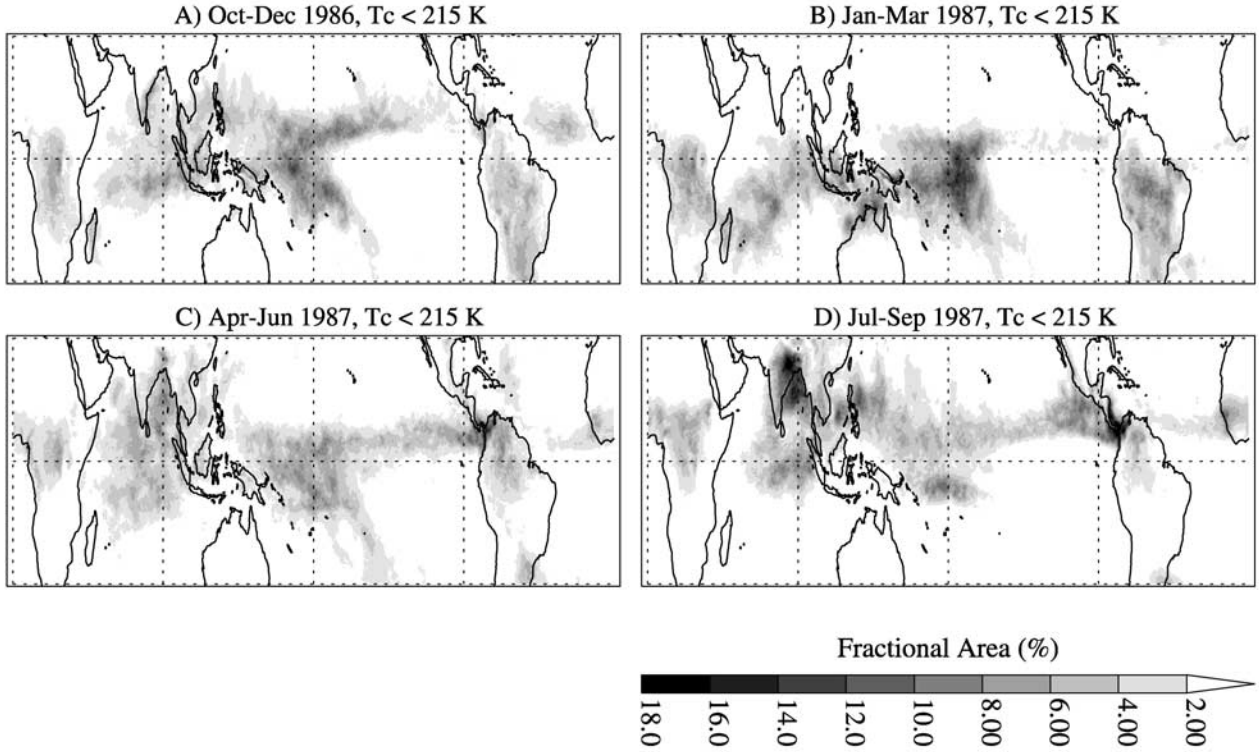


**Figure 3.** The distribution of convective events colder than 215°K ($\eta_{215}$) in percent, for each of four 3-month seasons: (a) October–December, (b) January–March, (c) April–June, and (d) July–September. Plot range is 30°S to 30°N.

(Figure 4a) than during August (Figure 4b). In each month, a small fraction of cloud (~0.5%) does appear colder than the mean tropopause. The maximum $\overline{\eta}(t)$ above the tropopause is about the same in each summer hemisphere. However, overshooting convection is colder and higher in February when the CPT is coldest.

[17] Figure 5 presents the distribution of the fraction of cloud colder than the CPT ($\eta_{CPT}$), for each of four seasons, with a similar convention as in Figure 3. Also superimposed are contours of seasonally averaged CPT temperature. Convective events colder than the environmental CPT are found in specific locations. Very few locations and seasons have $\eta_{CPT}$ greater than 1% (recall from the discussion in section 2.2 that this quantitative estimate is likely low by as much as 1% coverage). The largest values of $\eta_{CPT}$ in Figure 5, as for $\eta_{215}$ in Figure 3, are found over the Indian subcontinent and over Central America in July–September (Figure 5d). Oceanic convection penetrates the tropopause significantly in the central Pacific in January–March of this year (Figure 5b), which was an El Niño warm event. Large values of $\eta_{CPT}$ are found over the intertropical convergence zones, and also over the convective regions of central Africa, as well as over northern Australia during summer (Figure 5b). Many of these particular regions have been studied by field programs, and deep convection has been observed up to tropopause levels over northeast India [*Cornford and Spavins*, 1973], Central America [*Kley et al.*, 1982], and northern Australia [*Kritz et al.*, 1993].

[18] Convective events that penetrate the tropopause are broadly found in the same regions as deep convective activity in Figure 3, with some exceptions. Convection over tropical South America and over the Indian Ocean is rarely colder than the CPT. Yet the tropopause is anomalously cold over South America. The strong diurnal variations there limit $\eta_{CPT}$ by limiting cold cloud to only a few hours of the day. Almost all of the distribution is within 15°C of the tropopause, or within 1.5 km. This is similar to midlatitude observations of overshoots in severe storms [*Shenk*, 1974; *Roach*, 1966].

[19] Figure 5 highlights the relationship between $\eta_{CPT}$ and CPT temperatures. In general, there is good correspondence between the coldest tropopause temperatures and values of $\eta_{CPT}$ > 0.25%. Minima in CPT appear generally over equatorial Africa and South America, and over the western and central Pacific. In July–September (Figure 5d) a minimum in CPT also appears near the monsoon circulation over South Asia. In some cases, CPT minima appear adjacent to regions of significant $\eta_{CPT}$, such as the region of cold tropopause temperatures in October–December over South America without significant convection at these levels (Figure 5a). There are also asymmetries around the equator, for example, in October–December (Figure 5a), coldest tropopause temperatures are found in the Northern Hemisphere, while the largest values of $\eta_{CPT}$ are nearby but in the Southern Hemisphere.

[20] There is also significant interannual variability of convection reaching the tropopause. Figure 6 illustrates seasonal averages for December–February in 1988–1989 (a La Niña cold event) and December–February in 1991–1992 (an El Niño warm event). There are clearly big shifts in both the tropopause temperature and the location of convection that occur with El Niño, as noted previously by *Yulaeva and Wallace* [1994]. During 1991–1992, convection shifts from the western Pacific to the central Pacific, and the frequency of convective penetration increases there, as illustrated in Figure 6. In both of these years, there is good coincidence between the coldest tropopause temperatures and the largest fraction of deep convection reaching to these levels. We investigate this coincidence further in the next section.

## 4. Convection and the Tropopause

[21] We now investigate in more detail the relationship between convection and the tropopause, in coherent spatial variations of GCI and analyzed tropopause. We use variations over the diurnal

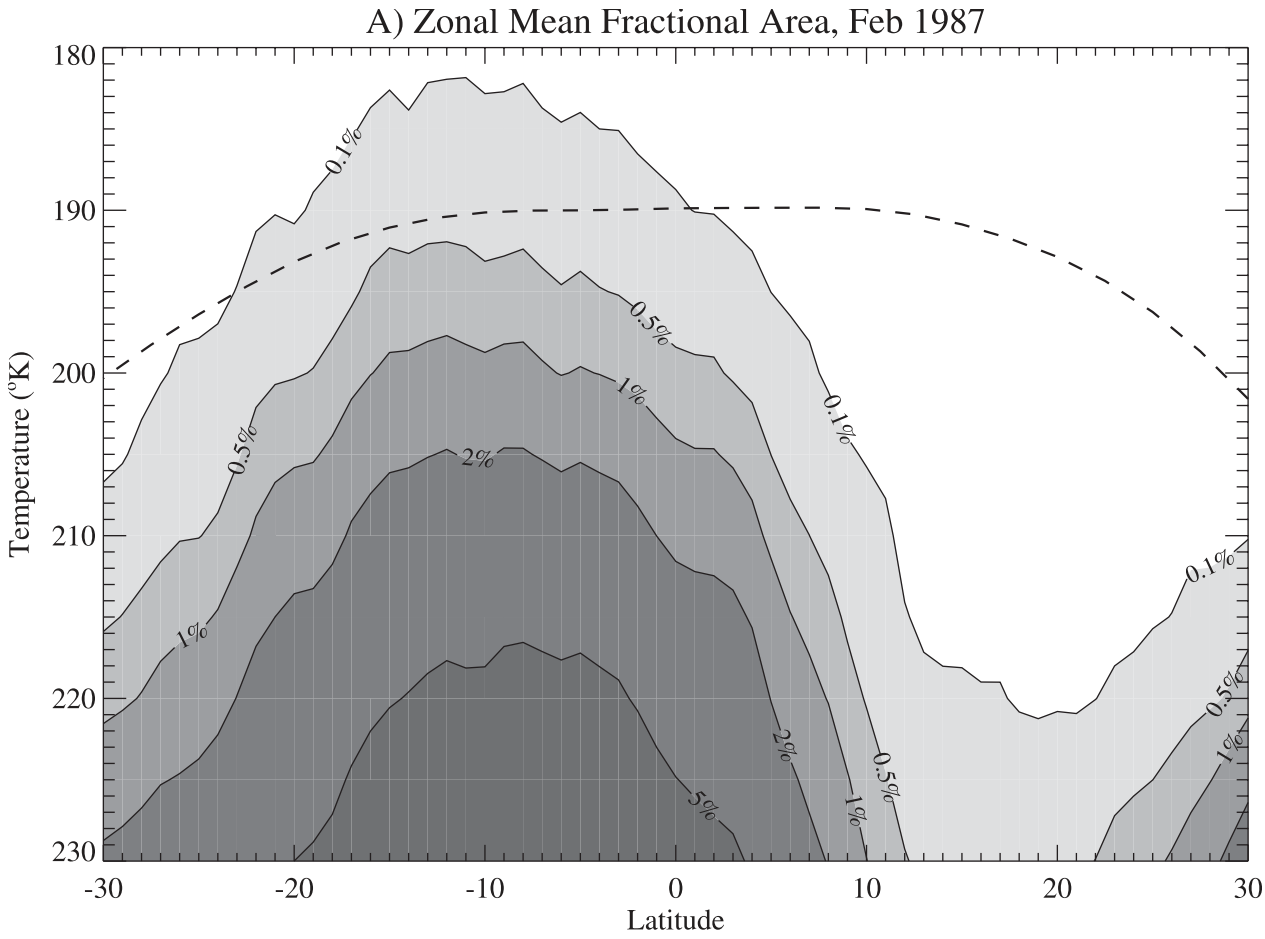


**Figure 4.** The zonal mean vertical distribution of convective events ($\overline{\eta}$) as a function of latitude and temperature for (a) February and (b) August. Thick dashed lines are the monthly averaged zonal mean cold point tropopause temperature.

cycle and the statistics of coincident GCI and CPT temperature measurements.

[22] The joint probability distribution of GCI brightness temperature and coincident CPT tropopause temperature is illustrated in Figure 7 for February and August, between 20°S to 20°N. The probability distribution is presented as cloud fraction, $\eta$ (in percent), for a given bin of tropopause and GCI temperature. The solid line marks where the GCI temperature equals the analyzed CPT temperature. Above this line, clouds are colder than the CPT. No clouds are colder than the tropopause for tropopause temperatures warmer than 195°K in February and warmer than 200°K in August. However, the coldest CPT is accompanied by clouds colder than the tropopause. In February (Figure 7a), the fraction of clouds above the tropopause increases sharply as tropopause temperature decreases. Their joint occurrence suggests a relationship between overshooting convection and the coldest tropopause temperatures. It echoes a similar relationship observed during Monsoon Experiment (MONEX) [*Johnson and Kriete*, 1982].

[23] Figure 7 implies a relationship between the deepest convection and the cold point consistent with Figure 5. Convection near and at the local tropopause is not found in regions of warm tropical tropopause temperatures. On the other hand, convection above the tropopause is strongly related to tropopause temperature, especially in February (Figure 7a) when tropopause temperatures are coldest. The relationship is consistent with the significant correlation between higher tropopause height and decreased middle (800–300 hPa) tropospheric stability (convective mixing) in monthly mean radiosonde data by *Seidel et al.* [2001], though a significant correlation with tropopause temperatures was not obtained with monthly mean data. Two interpretations are possible. One is that convection acts to cool the tropopause. Another interpretation of Figure 7 is that a colder tropopause may reduce the stability of the upper troposphere and raise the level of neutral buoyancy of convection.

[24] A second approach to the relationship between convection and the tropopause is to focus on the coherence of the diurnal cycle of both quantities. In Figure 8 the diurnal cycle of tropopause temperature and the diurnal cycle of $\eta_{CPT}$ are examined for an active convective region over land. The GCI has been smoothed in time with a 1-2-1 filter to better compare 3 hourly GCI data with 6 hourly tropopause data. Over South America the tropopause temperature (Figure 8a) is a minimum at 2000 local time (LT)(0000 UTC). The $\eta_{CPT}$ value peaks at 1700 local time (Figure 8b), ~3 hours prior. Hence the coldest, highest tropopause appears shortly after the maximum overshooting convection.

[25] The diurnal range of tropopause temperature is ~1.5°C (Figure 8). The $\eta_{CPT}$ value increases by a factor of 3 between its minimum at 0800 LT and its maximum at 1700 LT. Other tropical land regions (such as Africa) exhibit similar diurnal patterns of tropopause temperature and $\eta_{CPT}$. The timing of convective activity above the tropopause is consistent with the diurnal cycle of convection over land that peaks in the evening. It is also consistent with the diurnal cycle of deep convection above the tropopause over South America presented by *Soden* [2000].

[26] The diurnal cycles of CPT temperature and $\eta_{CPT}$ are consistent with the joint statistics of Figure 7 and with colder cloud tops occurring in regions of colder tropopause temperatures.

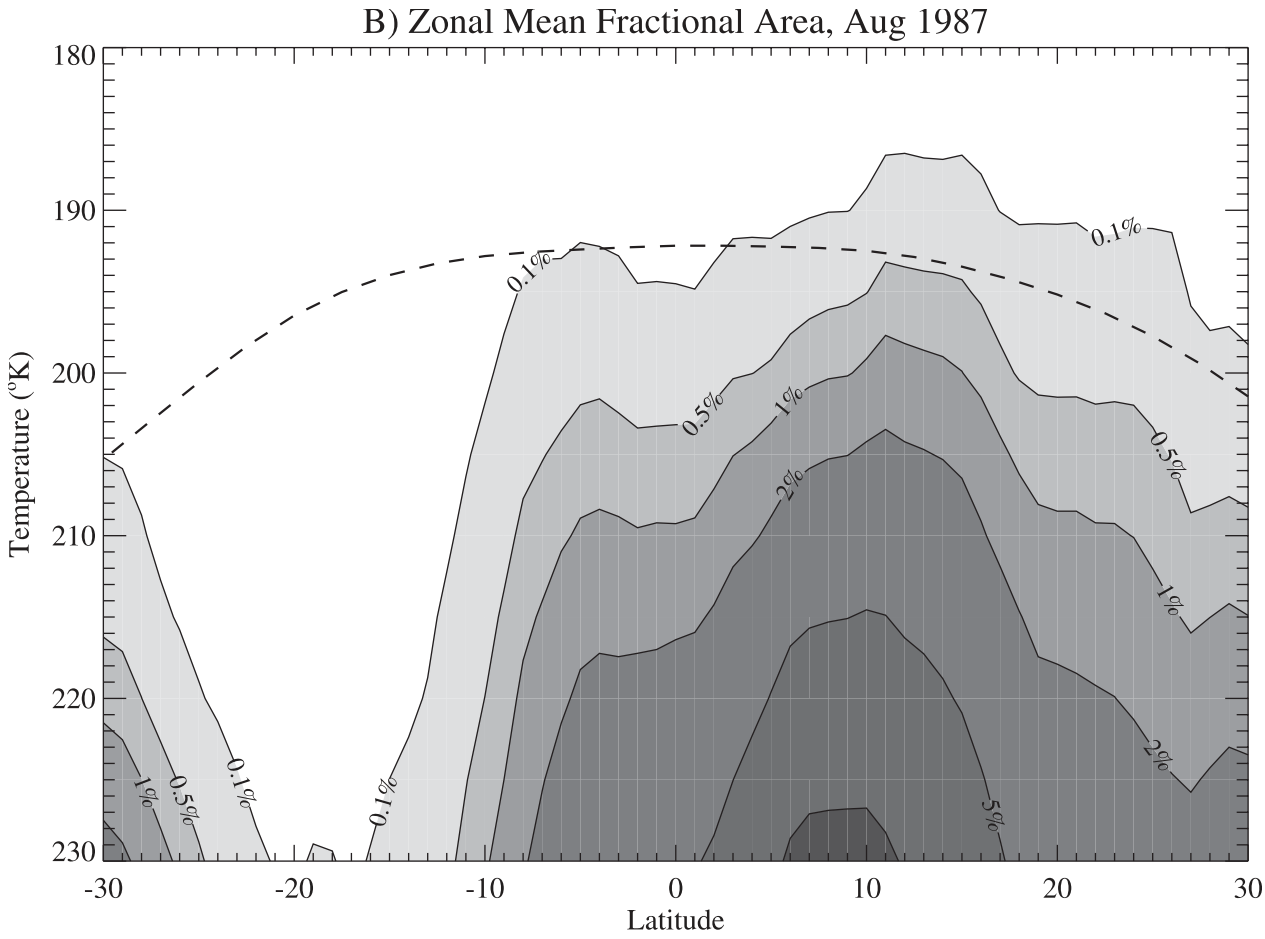


**Figure 4.** (continued)

Over oceanic regions, there is little evidence of a diurnal cycle of tropopause temperatures, and convection tends to peak in the morning (local time). As illustrated in Figure 5, $\eta_{CPT}$ is generally higher over oceanic regions than over land, particularly in October–December and January–March.

[27] Differences between land and ocean are further investigated by correlations between time series of GCI and tropopause temperature. Linear correlations were calculated between the GCI brightness temperatures and the coincident analyzed CPT temperatures over several regions. In most regions, correlations greater than ±0.5 exist only over land. Correlations were generally lower over the oceans.

[28] The GCI brightness temperatures and analyzed tropopause temperatures were also filtered to highlight the diurnal cycle and to highlight lower-frequency variability at periods longer than 7 days. Correlations with a diurnal bandpass filter are particularly strong over land (as high as 0.8) and are not strong over the oceans. Even low-pass filtered time series do not show high correlations over oceanic regions. These correlations were qualitatively consistent whether broad regional averages or individual points were analyzed.

[29] Oceanic convection, while reaching the tropopause, exhibits less of a relationship to the tropopause than does continental convection. However, oceanic convection reaches the tropopause more frequently. This discrepancy can be accounted for by noting that convection over land is less frequent and occurs throughout the day, whereas oceanic convection occurs at many local times. Additionally, an analysis of radiosondes indicates that during active convective seasons, the stability in the tropopause region is higher over South America than over the western Pacific. The differences, integrated over 12–16 km, are as much as 500 J kg$^{-1}$ in buoyancy units, or as much as 10–25% of the total integrated parcel buoyancy (commonly called the convective available potential energy) in a sounding. Thus the tropopause region over South America is more stable and "resistant" to convective penetration than over the western Pacific.

## 5. Convective Turnover Time

[30] We now use the cloud behavior to deduce a tentative estimate of the rate at which air is transferred into the tropopause region by convection. The convective turnover time ($\tau_c$) characterizes the time for convection to replace the air mass in the tropopause region. The $\tau_c$ value is subject to a number of uncertainties that we quantify here and in the Appendix A.

[31] The turnover time ($\tau_c$) is estimated using the following method. First, the temperature difference between an individual GCI cloud observation and a specified environmental temperature (180° to 230°K) is converted to a pressure difference ($dp$). The approximate pressure and altitude ($z$) for specified environmental temperatures is based on a mean atmospheric sounding in the Western Pacific, where convection is ubiquitous.

[32] Using the hydrostatic relation, the mass in a column ($m_c$) is found from $m_c = \rho\Delta z = -dp/g$, where $\rho$ is density and $g$ is the gravitational acceleration. The $m_c$ value is multiplied by the area of a GCI pixel ($A$), yielding the total mass of cloud observed above the environmental temperature level in one GCI pixel. The mass is assumed to have filled the volume in 3 hours, the time interval of the GCI input data (which gives a timescale for the flux). The

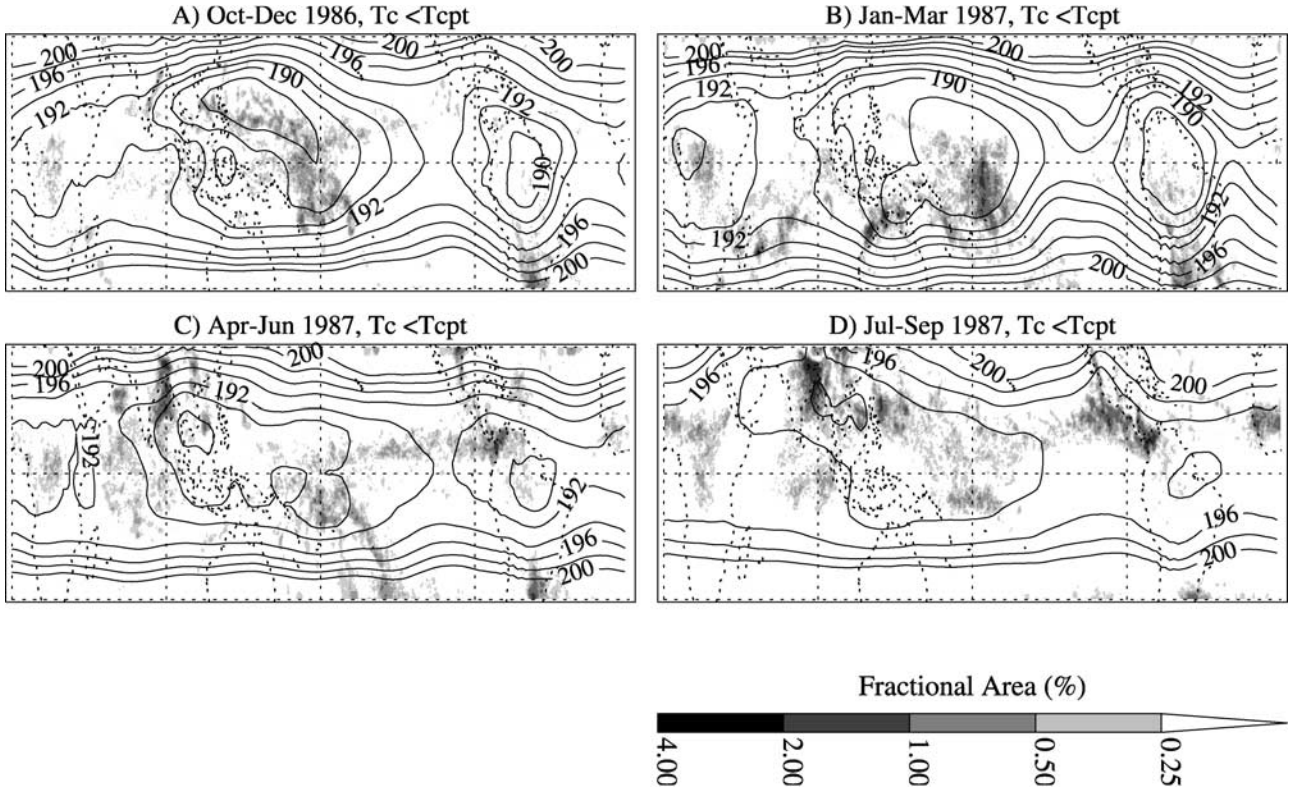


**Figure 5.** The distribution of convective events colder than the cold point tropopause ($\eta_{CPT}$) for each of four 3-month seasons: (a) October–December, (b) January–March, (c) April–June, and (d) July–September. Plot range is 30°S to 30°N. Thin black lines are seasonally averaged analyzed CPT temperature. Contour interval is 1°K from 187° to 192°K and 2°K from 192° to 200°K.

individual columns ($m_c$) can be calculated at the altitude of each environmental temperature, yielding $m_c$ as a function of height ($m_c(z)$), which can be summed over a time $T$ and a region $R$ to estimate the summed convective flux $F_c(z) = \Sigma^T\Sigma^R m_c(z)A$. Because the summed convective flux ($F_c(z)$) contains millions of pixels, this statistic of convective overshoots has reduced uncertainty relative to the individual convective events (see Appendix A). We then define the mass of a layer between a reference temperature and 50 hPa (19 km, or 2–3 km above the cold point) as $M_R$. Finally, the "turnover time" is defined as $\tau_c(z) = M_R(z)/F_c(z)$. The $\tau_c$ value has units of time and measures the rate at which air in a region $M_R$ is replenished. The $\tau_c$ characterizes the source of lower tropospheric air at a given level introduced through cumulus detrainment and mixing.

[33] The estimate of timescales is subject to a number of uncertainties. These were described in section 2.2 and are detailed

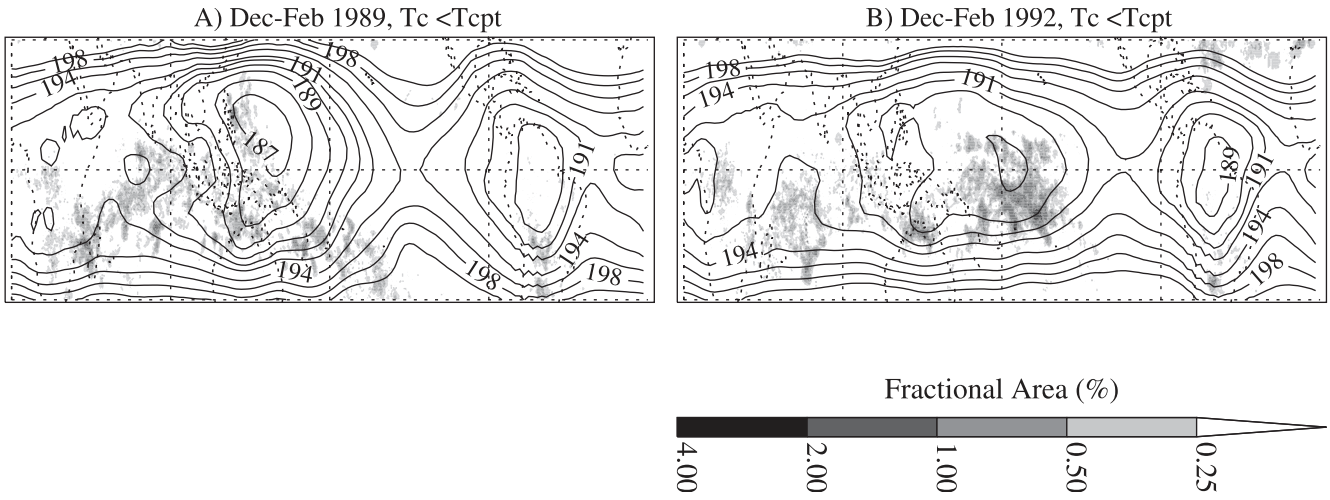


**Figure 6.** Cloud fraction above the tropopause ($\eta_{CPT}$) during (a) December 1988–February 1989 and (b) December 1991–February 1992. Thin contour lines are monthly mean tropopause temperature. Contour interval is 1°K from 187° to 192°K and 2°K from 192° to 200°K.

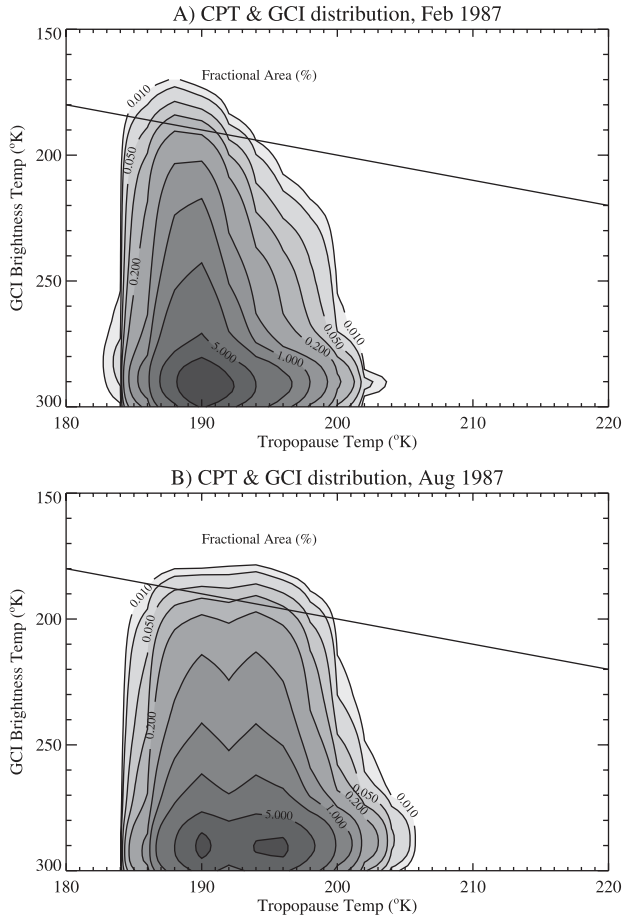


**Figure 7.** Distribution of GCI brightness temperatures ($T_c$) as a function of coincident cold point tropopause temperature ($T_{CPT}$) for tropical points between 20°S and 20°N: (a) February and (b) August. Solid line is the 1:1 line ($T_c = T_{CPT}$).

in the Appendix A. We will summarize these uncertainties again here. Using the stochastic model of cloud (Appendix A), we can estimate these uncertainties by performing a calculation of $F_c$ and comparing the summed fluxes derived for the actual simulated distribution at 1km and 6-min resolution ($F_c^a$) and the same distribution sampled at the time and space scales (3 hours and 50 km) of the GCI data ($F_c^s$). The distribution of clouds was generated so that the histogram closely matched the observed histogram (Figure 2).

[34] The loss of resolution in the GCI data for cold temperatures (Figure 2) results in an underestimate of $F_c$ that increases with height. At temperatures of 220°K and warmer (altitudes of 12 km and below) there is virtually no difference between $F_c^a$ and the estimate $F_c^s$. However, $F_c^s$ is nearly 30% less than $F_c^a$ at 200°K. By 195°K, $F_c^s$ is less than $F_c^a$ by 100% and by 200% at 185°K. That is, the actual mass flux at these levels can be 2–3 times greater than the flux represented by the limited satellite sampling. Furthermore, the comparatively coarse temporal sampling introduces uncertainties in $F_c^s$ ranging from ±30% at 220°–240°K to 50% or more at tropopause levels.

[35] In addition to the uncertainties on $\tau_c$ already discussed, in order for air in convective towers (with low potential temperature or θ) to remain at tropopause levels (high θ) and not sink, it must mix with higher θ surrounding air. This means for cloud to irreversibly transport air into the tropopause region, it must contain some proportion (10–60%) of higher θ tropopause region air. This would represent an anvil cloud after mixing. Thus the actual source of tropospheric air into the tropopause region may be less than estimated by the turnover time because some of the air is from the tropopause region itself. On the basis of cloud entrainment models [*Grabowski*, 1995] and theoretical studies [*Scorer*, 1978], we estimate this mixing might reduce $F_c$ by 10–60% and increase the turnover time.

[36] Figure 9 presents an estimate of $\tau_c(z)$ as a function of altitude. The estimates have been corrected for the underestimation from spatial sampling at each level, and error bars are plotted at each level based on uncertainties due to temporal sampling. Mixing of tropopause region air has not been accounted for. Uncertainties of ±5°C would shift the curve up or down by 1 km, not changing the basic qualitative results. At the base of the tropopause region, around 11–12 km, turnover times are shorter than 1 month, and they increase exponentially with altitude. The $\tau_c$ exceeds a year at 16 km or 100 hPa. Above ~14 km, there are significant seasonal differences, with a shorter turnover time (more convection) in January–March, and the longest turnover time in July–September. These differences are most pronounced where the calculation is most uncertain above 100 hPa.

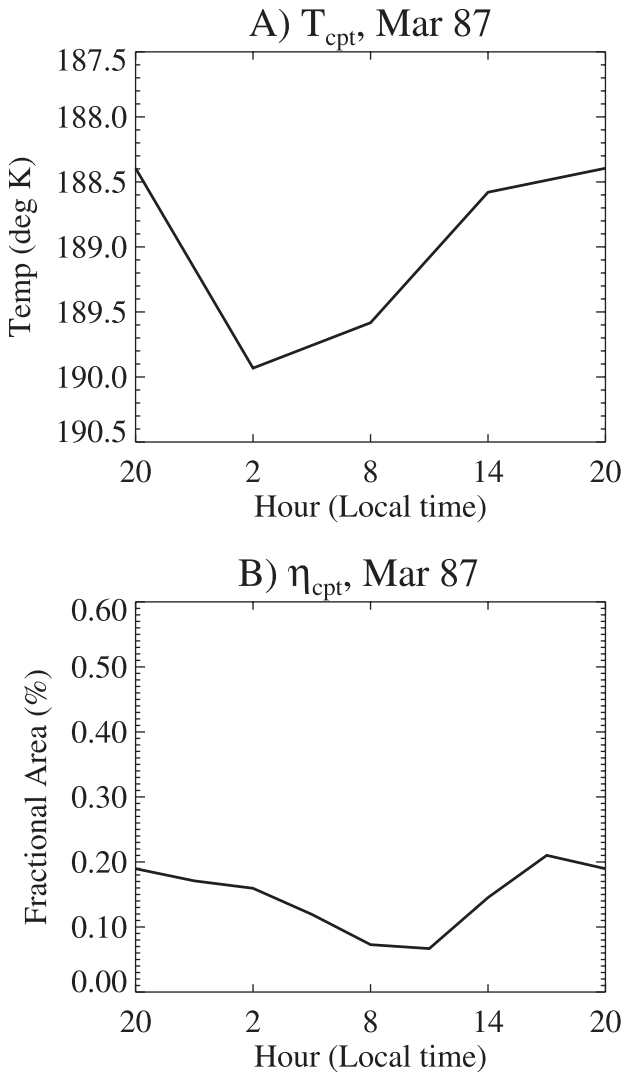


**Figure 8.** Diurnal cycles over South America (20°S–0 and 280°–320°E) in March: (a) Cold point tropopause temperature ($T_{CPT}$), and (b) fractional area of convection colder than the tropopause, $\eta_{CPT}$.

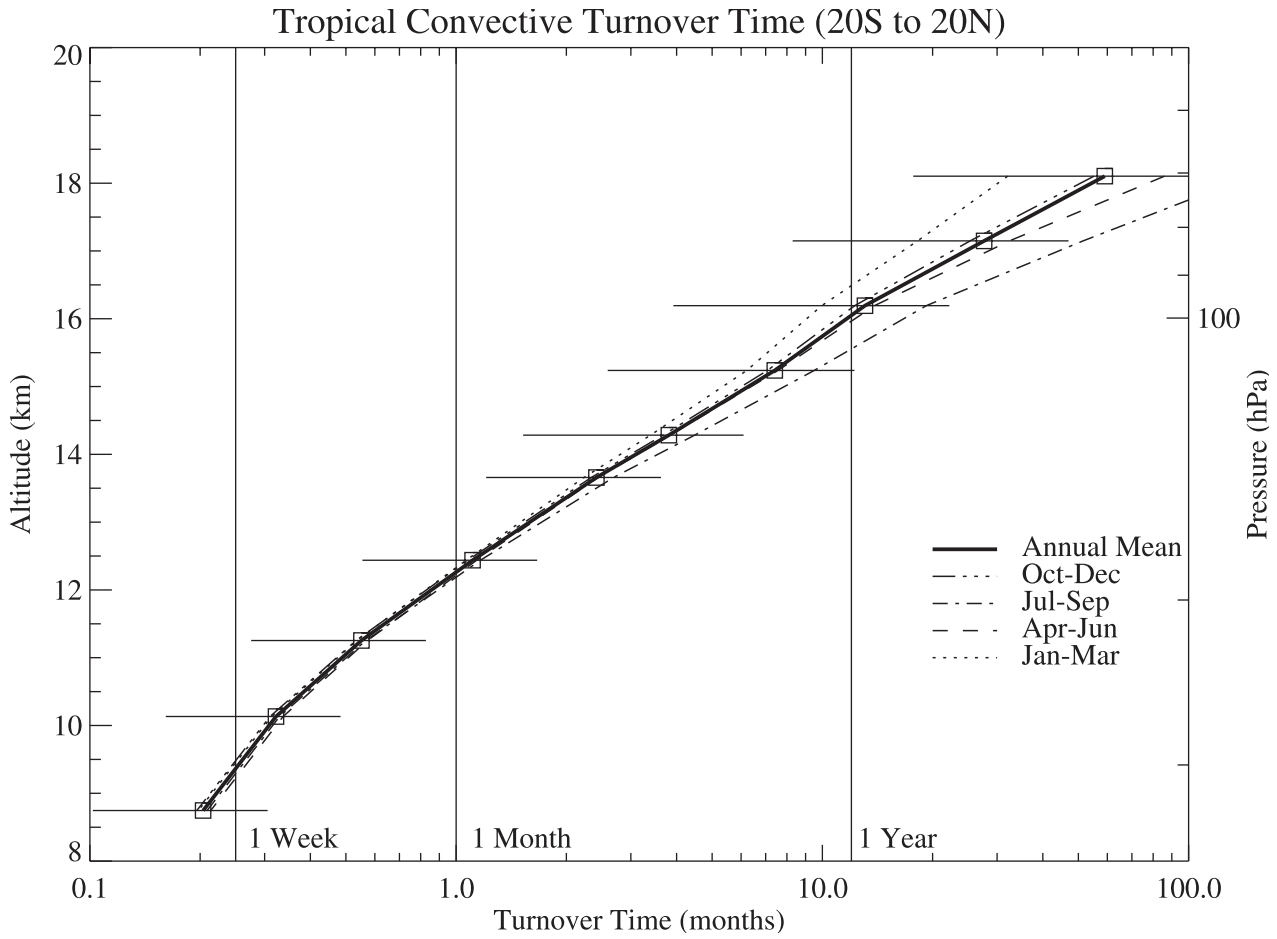


**Figure 9.** Global tropical convective turnover time, $\tau_c$, in months as a function of height and pressure. Annual mean shown as a thick solid line, October–December mean as a dash-dot-dot-dot line, July–September mean as a dash-dot line, April–June as a dashed line, and January–March as a dotted line. Horizontal lines indicate error bars.

[37] For illustration of some of the regional differences evident in Figures 3 and 5, the calculation of $\tau_c$ is repeated for different regions of the tropics in Figure 10. This calculation includes only vertical transport of air in convection. It does not include horizontal advection of air in the tropopause region which may have been recently processed by convection somewhere else. Nonetheless, it illustrates significant regional and vertical differences in the influence of convection. Less convection (longer turnover time) is found in the Atlantic and eastern Pacific. Below 14 km, the shortest convective turnover time is over the Indian subcontinent and Indian Ocean. But above 14 km, the shortest $\tau_c$ is located in the western and central Pacific Ocean, where clouds are coldest and highest.

## 6. Discussion and Conclusions

[38] Deep convection reaches up to the tropopause in the tropics. Zonally averaged cloud fraction in the tropopause region is just a few percent. Although the fractional coverage above the tropopause is small, it appears to have a strong effect on the tropopause.

[39] The distribution of convection above the tropopause ($\eta_{CPT}$) is similar to that of convection reaching the base of the tropopause region ($\eta_{215}$). Globally, convection above the tropopause is highest in Northern Hemisphere winter, in the summer hemisphere. Regionally, convection is strongest and deepest over the central and western Pacific in February, and over the Indian Monsoon in August. Statistically, convection rarely penetrates less than 1.5 km above the cold point tropopause. There are also large interannual changes in convection in the tropopause region, especially in the Pacific ocean. These changes are associated with changes in convection due to El Niño events. These changes may have a big effect on the interannual variation of water vapor entering the stratosphere. As further years of data become available, the interannual variability should be investigated.

[40] There is a strong relationship between deep convection and the tropopause. The spatial-temporal analyses indicate that there is a significant correspondence between the deepest convection and coldest tropopause temperatures on both large and small scales. The relationship is stronger in boreal winter (February) than in boreal summer (August). These relationships are either a result of convective cooling of the tropopause, or a tropopause cooled by other means (such as radiative cooling) permitting deeper convection. The former appears more likely, but the issue deserves further investigation. In addition there are coherent diurnal cycles of tropopause and clouds at and above the tropopause level. Those cycles are stronger and clearly related over land, where the tropopause is coldest after the evening peak of local convection

[41] The convective turnover time in the tropopause region is on the order of weeks below 12 km, increasing to months at 13–14 km, and a year or more at 16 km and above. Uncertainties are large at 100 hPa (16 km) and above because $\eta$ is

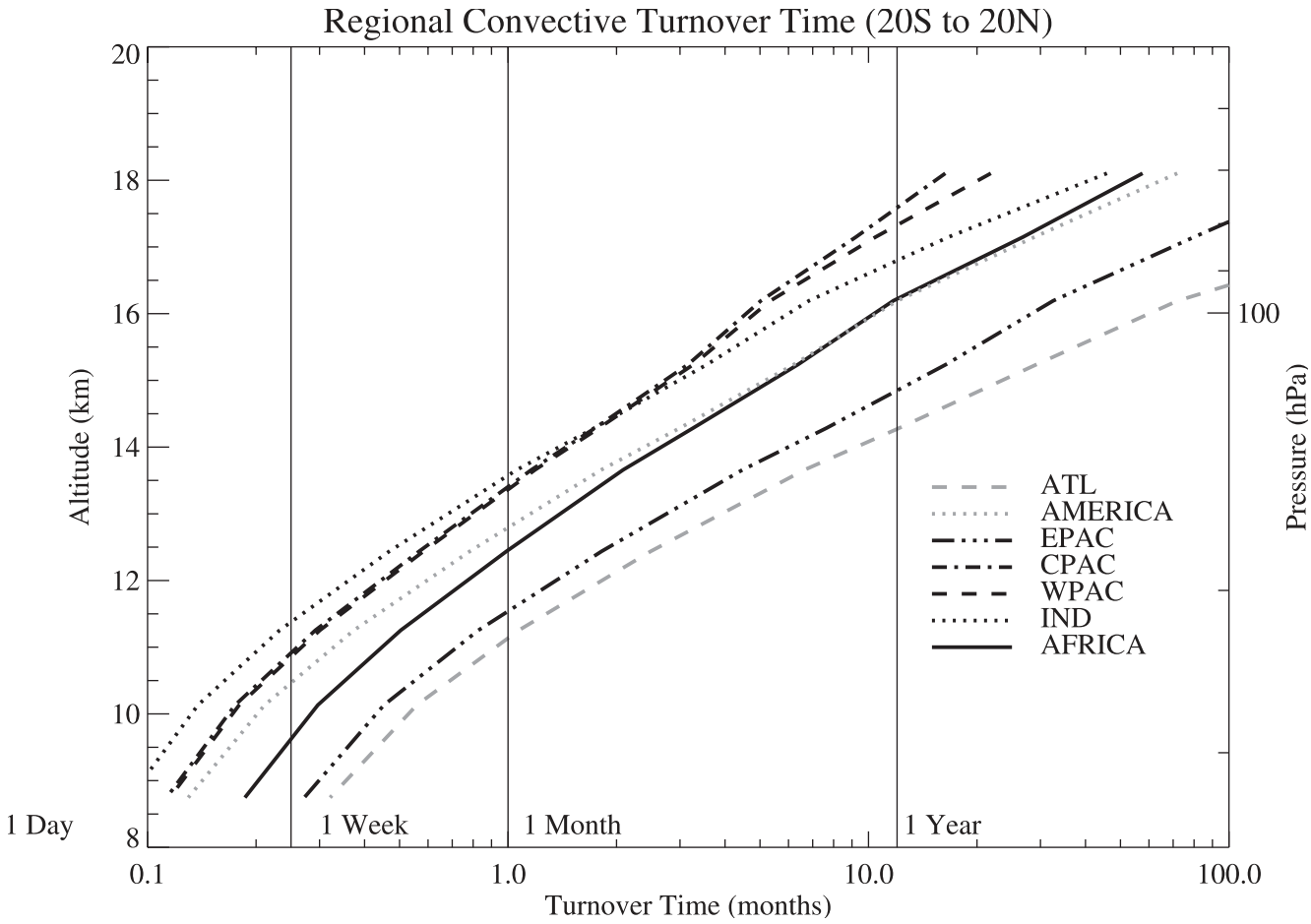


**Figure 10.** Regional tropical convective turnover time, $\tau_c$, in months as a function of height and pressure. Annual mean shown for different regions. Africa (0°–50°E) solid line, Indian Ocean (50°–110°E) dotted line, western Pacific (110°–170°E) dashed line, central Pacific (170°E–140°W) dash-dot line, Eastern Pacific (140°–90°W) dash-dot-dot-dot line, South America (90–40W) gray dotted line, and Atlantic (40°–0°W) gray dashed line.

small. There are regional differences too, which indicate that the convective source of air at tropopause levels is more rapid in the western and central Pacific than elsewhere. Below 14 km however, the convective turnover time is shortest in the Indian Ocean. These regional estimates will be affected by horizontal advection.

[42] These results lead to some interesting observations about the exchange of air between the troposphere and stratosphere. There is a significant correspondence locally between the deepest convection and coldest tropopause temperatures on small and seasonal scales (Figure 5). However, the deep convection is displaced into the summer hemisphere (Figure 4), while the lowest tropopause temperatures are more symmetrical about the equator. There are also regions of cold tropopause temperatures without significant convection reaching these levels. Those regions, however, usually lie adjacent to regions with convection at tropopause levels. The relationship may result from horizontal transport of convectively processed air, and/or a large-scale dynamic response to the tropospheric release of latent heat in convection.

[43] The analysis of convective exchange and turnover time in section 5 indicates that convection rapidly supplies air to the upper troposphere and to the base of the tropopause region. Given a radiative heating rate in the tropopause region of 0.5°K day$^{-1}$ [e.g., *Schoberl et al.*, 1998], and a vertical displacement across the tropopause region of ~40°K (350°–390°K) in potential temperature units, this implies a timescale for radiative transport of 80 days or nearly 3 months. The estimates of $\tau_c$ derived here indicate, that above 15–16 km, radiation becomes more important for vertical motion than convection. However, beneath this altitude, convective mixing dominates.

[44] This has been an exploratory study with many uncertainties. Similar studies are possible with locally higher resolution data (from the TRMM satellite for example), but not with the coverage and continuity possible here. Major uncertainties exist in interpreting any of these data, particularly in quantifying the effect of convection on the tropopause. Higher-resolution analyses and further detailed in situ observations in the tropopause region will be necessary to reduce the uncertainties, and validate these conclusions regarding convection and stratosphere-troposphere exchange.

## Appendix A

[45] We divide the discussion of uncertainties in this appendix into sampling uncertainties (section A1) and uncertainties in locating the cloud top with brightness temperature measurements (section A2).

### A1. Sampling Uncertainties

[46] A Monte Carlo simulator for convection was built to quantify the sampling issues involved in the estimation of fractional cloud coverage and turnover time. The process mimics the

sampling that goes into the GCI data; acquisition of 8-km pixels at certain times from a higher-resolution grid and then subsequent averaging into the GCI pixels, sampled only a few times in 3 hours. The simulator creates distributions of cloud and overshoots on a 1km grid spanning 64 km. These distributions are created with a base level, a cloud top level and a possible overshoot level at high time resolution, such as 5–10 min. Clouds persist from one time to the next, with stochastically varying temperature and horizontal size, and a random probability of dissipating with an expected lifetime of 120 min.

[47] An example of the results from the simulator for one GCI pixel at one time is illustrated in Figure 11a, showing the 1km "actual" distribution (gray line), and the 8-km "observed" distribution (dotted line). The GCI sampling is represented as the average of the 8-km distribution over the whole domain (dashed). The average of these individual snapshots at 6-min intervals is indicated in Figure 11b. The solid gray line is a 6-min average of 64 1-km observations and the dotted line in Figure 11b is the average of 8-km pixels at each 6-min interval. The GCI value for this pixel over 3 hours is the average of the 8-km pixels at one time, in this case, 96 min (the vertical line in Figure 11b). In Figures 11a and 11b this value is indicated by the horizontal dashed line. For simplicity, the model is developed in one spatial dimension, but, in principle, two spatial dimensions would yield a similar result.

[48] Distributions of convection are selected to resemble histograms from observations (convective cloud heights are sampled from a gamma distribution of order 2). The parameters (probabilities) for the creation of cloud and overshoots are tuned so that the low temperature tail of the histograms resembles the observed tail in Figure 2. As observed, the average histogram is lower at both ends and higher in the middle of the distribution than the higher-resolution data. The model is not very sensitive to the details of the cloud distribution. The model has been run for 10,000 interactions (pixels) to generate statistics.

[49] Coarse spatial sampling results in a slight overestimation of temperature (the actual distribution in Figure 11b has a mean of 224°K, and the 8-km resolution data a mean of 225°K). The temporal sampling introduces an uncertainty into the estimated temperature. In Figure 11b the estimate (229°K) is warmer than the mean, but it could be equally a colder temperature. Multiple runs indicate that the uncertainty in estimating cloud fractions due to coarse temporal sampling (such as in Figure 2b) is approximately ±10% at temperatures warmer than 230°–240°K. However, this increases to ±30% in the tropopause region.

[50] The volumetric method described in section 5 is used to calculate summed convective fluxes ($F_c$) above given thresholds. Summed convective fluxes are calculated from the actual distribution ($F_c^a$) using 1-km pixels every 6 min and the 8-km averaged distribution. The summed fluxes estimated from the 8-km data sampled at high temporal resolution are only 5% lower than $F_c^a$. A GCI "sampled" flux ($F_c^s$) is calculated using temperatures sampled at only a few times from the 8-km data and averaged over a pixel before calculating the flux, equivalent to the sampling of the GCI data, and $F_c(z)$ described in section 5. The difference between $F_c^a$ (actual) and $F_c^s$ (sampled) enables us to quantify spatial and temporal sampling uncertainties. $F_c^s$ is nearly equal to $F_c^a$ at levels up to 230°K or so. $F_c^s$ decreases to ~50% of $F_c^a$ at tropopause levels (190°K), and continues to decrease at lower temperatures. These numbers are not that sensitive to the description of convective overshooting, but mostly sensitive to the overall area of the larger cloud deck (an anvil cloud in this conceptualization).

[51] We use these numbers to modify the turnover time estimates (Figure 9) and place error bars on them. Between 230°K and the tropopause $F_c^s$ is increased from the GCI estimate by adding a correction factor from zero at 230°K, to 100% at the tropopause (190°K) and 200% above (to correct for the fall off noted above).

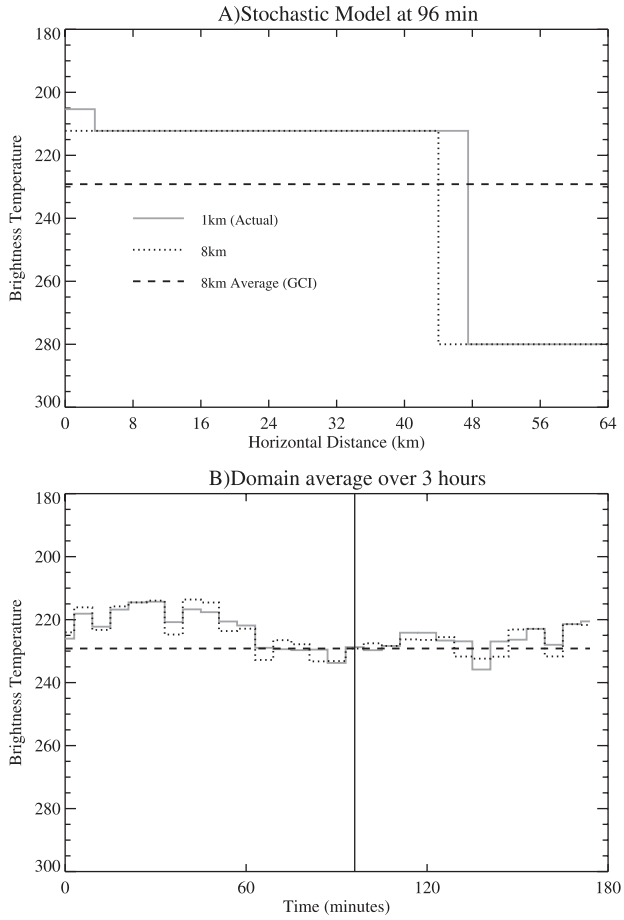


**Figure 11.** Sample output from stochastic simulator of cloud distributions. (a) Sample cloud field for one time. (b) Spatially averaged brightness temperature as a function of time. The solid gray line is the average of the actual field (1-km resolution). The dotted line is the spatial average of the sampled 8-km distribution, and the dashed line is the GCI average taken by sampling the 8-km distribution at only one time (the time depicted in Figure 11a and the vertical line in Figure 11b).

This shortens the estimated turnover time in the tropopause region. Uncertainties are large in this region where corrections are applied, and error bars are 70% of the estimate. At levels warmer than 230°K (below 12 km), uncertainties of 50% are derived from uncertainties in the altitude of the clouds and the low temporal frequency of sampling. The uncertainties include the effects of (1) a fall off in sensitivity at low temperatures (Figure 2), (2) temporal sampling only once or twice in 3 hours, and (3) spatial averaging before sampling. The uncertainties do not include mixing with environmental air.

### A2. Cloud Top Uncertainties

[52] In addition to sampling uncertainties are uncertainties in estimating cloud top with brightness temperature. We note first that brightness temperature does not measure exact cloud top but, rather corresponds to the IR emission temperature of approximately one optical depth below cloud top. For convective towers and anvils the IR emission level has been estimated at 0.5–1 km below cloud top [*Heymsfield et al.*, 1991]. At near adiabatic lapse rates this means that brightness temperature can be up to 9°C warmer than anvil tops. Brightness temperature data in the tropopause region do not accurately represent thin cirrus or thin anvil, which are interpreted as being warmer and lower.

[53] Clouds above their level of neutral buoyancy (LNB) are also colder than their environment. Comparing the brightness temperature of those clouds with an environmental temperature like the CPT is not straightforward, because a cloud will be colder than its environment. To account for this uncertainty, we use a parcel model of radiosonde observations from several tropical island and land stations to calculate the LNB and assume nearly adiabatic ascent above it. The parcel model assumes no entrainment and ascent at a constant near-adiabatic lapse rate. Statistics from several thousand soundings indicate that when the simulated parcels reached CPT temperatures they were actually 300–600 m below the tropopause. When the parcels overshooting their LNB reached the altitude of the CPT, the parcel temperatures were actually 2°–5°C colder than the analyzed CPT temperature. Also relevant is local modification of the tropopause on the scale of individual convective clouds, which is not resolved in the analyzed temperature fields. Clouds modify the local tropopause, as observed by the daily changes in temperature at tropopause levels associated with convective events [*Johnson and Kriete*, 1982, Figure 3]. The parcel model indicates that on average this effect is a few degrees of cooling in active convection regions. This cooling is equivalent to the effect of mixing the surrounding clouds into the local environment.

[54] Note that these two systematic errors in locating the height of cloud top from brightness temperatures act in different directions. Cloud tops are generally warmer than their brightness temperature, but clouds above their LNB are generally colder than their environment. Thus when averaged over many individual pixels in time and space, the observed IR brightness temperature may be a reasonable estimator of cloud top height when compared to environmental temperatures.

[55] **Acknowledgments.** Thanks to J. Kelly for assistance with high resolution GCI data. We would also like to thank J. McGinley, A. Heymsfield, A. Crook, and M. Moncrieff for their insights into the organization of tropical convection and its radiative properties, and R. Garcia and B. Boville for their comments. The National Center for Atmospheric Research is operated by the University Corporation for Atmospheric Research under the sponsorship of the National Science Foundation. A. Gettelman was supported at NCAR by the Advanced Study Program, the Atmospheric Chemistry Division and the Climate and Global Dynamics Division.

## References

Atticks, M. G., and G. D. Robinson, Some features of the structure of the tropical tropopause, *Q. J. R. Meteorol. Soc.*, *109*, 295–308, 1983.

Bergman, J. W., and M. L. Salby, Equatorial wave activity derived from fluctuations in observed convection, *J. Atmos. Sci.*, *51*, 3791–3806, 1994.

Brewer, A. W., Evidence for a world circulation provided by the measurements of helium and water vapor distribution in the stratosphere, *Q. J. R. Meteorol. Soc.*, *75*, 351–363, 1949.

Cornford, S. G., and S. Spavins, Some measurements of cumulonimbus tops in the pre-monsoon season in north-east India, *Meteorol. Mag.*, *102*, 314–332, 1973.

Danielsen, E. F., A dehydration mechanism for the stratosphere, *Geophys. Res. Lett.*, *9*, 605–608, 1982.

Dobson, G. M. B., A. W. Brewer, and B. Cwilong, The meteorology of the stratosphere, *Proc. R. Soc. London, Ser. A*, *185*, 144–175, 1946.

Fujita, T. T., The mystery of severe storms, *WRL Res. Pap. 239*, Wind Res. Lab., Univ. of Chicago, Chicago, Ill., 1992.

Grabowski, W. W., Entrainment and mixing in buoyancy-reversing convection with applications to cloud top entrainment, *Q. J. R. Meteorol. Soc.*, *121*, 231–253, 1995.

Heymsfield, G. M., R. Fulton, and J. D. Spinhirne, Aircraft overflight measurements of midwest severe storms: Implications on geosynchronous satellite interpretations, *Mon. Weather Rev.*, *119*, 436–456, 1991.

Highwood, E. J., and B. J. Hoskins, The tropical tropopause, *Q. J. R. Meteorol. Soc.*, *124*, 1579–1604, 1998.

Hoinka, K. P., Statistics of the global tropopause pressure, *Mon. Weather Rev.*, *126*, 3303–3325, 1998.

Holton, J. R., P. H. Haynes, A. R. Douglass, R. B. Rood, and L. Pfister, Stratosphere-troposphere exchange, *Rev. Geophys.*, *33*, 403–439, 1995.

Johnson, R. H., and D. C. Kriete, Thermodynamic and circulation characteristics of winter monsoon tropical mesoscale convection, *Mon. Weather Rev.*, *110*, 1898–1911, 1982.

Kalnay, E., et al., The NCEP/NCAR 40-year reanalysis project, *Bull. Am. Meteorol. Soc.*, *77*, 437–471, 1996.

Kley, D., A. L. Schmeltekopf, K. Kelly, R. H. W. T. L. Thompson, and M. McFarland, Transport of water through the tropical tropopause, *Geophys. Res. Lett.*, *9*, 617–620, 1982.

Kochanski, A., Cross sections of the mean zonal flow and temperature along 80W, *J. Meteorology*, *12*, 95–106, 1955.

Kritz, M. A., S. W. Rosner, K. K. Kelly, M. Lowenstein, and K. R. Chan, Radon measurements in the lower tropical stratosphere: Evidence for rapid vertical transport and dehydration of tropospheric air, *J. Geophys. Res.*, *98*, 8725–8736, 1993.

Liebmann, B., H. H. Hendon, and G. D. Glick, The relationship between tropical cyclones of the western Pacific and Indian oceans and the Madden-Julian oscillation, *J. Meteorol. Soc. Jpn.*, *72*, 401–412, 1994.

Newell, R. E., and S. Gould-Stewart, A stratospheric fountain?, *J. Atmos. Sci.*, *38*, 2789–2796, 1981.

Randel, W. J., F. Wu, and D. J. Gaffen, Interannual variability of the tropical tropopause derived from radiosonde data and NCEP reanalyses, *J. Geophys. Res.*, *105*, 15,509–15,523, 2000.

Roach, W. T., An analysis of eight flights by U-2 aircraft over severe storms in Oklahoma, *Tech. Rep. ITERM-NSSL-29*, U.S. Dep. of Comm., Environ. Sci. Serv. Admin., Washington, D. C., 1966.

Roca, R., and V. Ramanathan, Scale dependence of monsoonal convective systems over the Indian ocean, *J. Clim.*, *13*, 1286–1298, 2000.

Salby, M. L., H. H. Hendon, K. Woodberry, and K. Tanaka, Analysis of global cloud imagery from multiple satellites, *Bull. Am. Meteorol. Soc.*, *72*, 467–480, 1991.

Sassi, F., M. Salby, and W. G. Read, Relationship between upper-tropospheric humidity and deep convection, *J. Geophys. Res.*, *106*, 17,133–17,146, 2001.

Schmetz, J., S. A. Tjemkes, M. Gube, and L. van de Berg, Monitoring deep convection and convective overshooting with METEOSAT, *Adv. Space Res.*, *19*(3), 433–441, 1997.

Schoberl, M. R., C. H. Jackman, and J. Rosenfield, A lagrangian estimate of aircraft effluent lifetime, *J. Geophys. Res.*, *103*, 10,817–10,825, 1998.

Scorer, R. S., *Environmental Aerodynamics*, John Wiley, New York, 1978.

Seidel, D. J., R. J. Ross, J. K. Angell, and G. C. Reid, Climatological characteristics of the tropical tropopause as revealed by radiosondes, *J. Geophys. Res.*, *106*, 7857–7878, 2001.

Selkirk, H. B., The tropopause cold trap in the Australian monsoon during STEP/AMEX 1987, *J. Geophys. Res.*, *98*, 8591–8610, 1993.

Shenk, W. E., Cloud top height variability of strong convective cells, *J. Appl. Meteorol.*, *13*, 917–922, 1974.

Sherwood, S. C., and A. E. Dessler, A model for transport across the tropical tropopause, *J. Atmos. Sci.*, *58*, 765–779, 2001.

Soden, B. J., The diurnal cycle of convection, clouds, and water vapor in the tropical upper troposphere, *Geophys. Res. Lett.*, *27*, 2173–2176, 2000.

Tanaka, K., K. Woodberry, H. Hendon, and M. Salby, Assimilation of global cloud imagery from multiple satellites, *J. Atmos. Oceanic Technol.*, *8*, 613–626, 1991.

Yulaeva, E., and J. M. Wallace, The signature of ENSO in global temperature and precipitation fields derived from the microwave sounding unit, *J. Clim.*, *7*, 1719–1736, 1994.

Zhang, C., On the annual cycle in highest, coldest clouds in the tropics, *J. Clim.*, *6*, 1987–1990, 1993.

Zhou, X., M. A. Geller, and M. Zhang, Tropical cold point tropopause characteristics derived from ECMWF reanalyses and soundings, *J. Clim.*, *14*, 1823–1838, 2001.

A. Gettelman and F. Sassi, National Center for Atmospheric Research, Box 3000, Boulder, CO 80307-3000, USA. (andrew@ucar.edu)

M. L. Salby, Program Atmospheric and Oceanic Sciences, University of Colorado, Boulder, CO 80309, USA.